Optically engineered ultrafast pulses for controlled rotations of exciton qubits in semiconductor quantum dots

Angela Gamouras, Reuble Mathew, and Kimberley C. Hall

Citation: Journal of Applied Physics **112**, 014313 (2012); doi: 10.1063/1.4731723
View online: http://dx.doi.org/10.1063/1.4731723
View Table of Contents: http://scitation.aip.org/content/aip/journal/jap/112/1?ver=pdfcov
Published by the AIP Publishing

Optically engineered ultrafast pulses for controlled rotations of exciton qubits in semiconductor quantum dots

Angela Gamouras, Reuble Mathew, and Kimberley C. Hall
Department of Physics and Atmospheric Science, Dalhousie University, Halifax, Nova Scotia B3H4R2, Canada

(Received 9 August 2011; accepted 30 May 2012; published online 6 July 2012)

Shaped ultrafast pulses designed for controlled-rotation (C-ROT) operations on exciton qubits in semiconductor quantum dots are demonstrated using a quantum control apparatus operating at ~1 eV. Optimum pulse shapes employing amplitude and phase shaping protocols are implemented using the output of an optical parametric oscillator and a programmable pulse shaping system, and characterized using autocorrelation and multiphoton intrapulse interference phase scan techniques. We apply our pulse characterization results and density matrix simulations to assess the fundamental limits on the fidelity of the C-ROT operation, providing a benchmark for the evaluation of sources of noise in other quantum control experiments. Our results indicate the effectiveness of pulse shaping techniques for achieving high fidelity quantum operations in quantum dots with a gate time below 1 ps. © *2012 American Institute of Physics*. [http://dx.doi.org/10.1063/1.4731723]

I. INTRODUCTION

Semiconductor quantum dots (QDs) are strong candidates for future solid state quantum computing architectures, in which the fundamental qubits may be realized using the quantum states of excitons or individual carrier spins.[1–13] Such an approach offers the promise of long term scalability through rapid advances in semiconductor growth and fabrication techniques, including tailored coupling via optical microcavity and waveguide modes,[7,11,13] as well as ease of integration with conventional computing technology. The possibility of manipulating the fundamental quantum states using optical techniques would exploit established photonic technologies, and may lead to THz operation rates. This potential has led to an intensive research effort in recent years dedicated to the pursuit of coherent optical control of quantum states in semiconductor quantum dots, including demonstrations of single qubit rotations involving excitons and single carrier spins,[14–22] entanglement,[23–25] adiabatic passage,[26,27] and quantum state tomography.[28]

Femtosecond pulse shaping techniques provide independent control of the temporal characteristics of the phase and amplitude of an optical pulse,[29] providing a means to tailor the light-matter interaction responsible for quantum control. The benefits of pulse shaping have been realized, for example, in the control of atomic and molecular systems[30–34] and chemical reactions.[35,36] It has recently been shown theoretically that the application of pulse shaping techniques to optically controlled quantum operations in semiconductor quantum dots can lead to substantial improvements in performance metrics such as gate fidelity and speed.[4,6,37] For these studies, the pulse shaping method was applied to the controlled-rotation (C-ROT) operation involving exciton qubits, representing a useful prototype for the general application of shaping techniques to optical control of charge and spin states in semiconductor quantum dots. The C-ROT operation is achieved using a four-level system consisting of the vacuum ground state $|00\rangle$, two exciton states $|01\rangle$ and $|10\rangle$, and the biexciton state $|11\rangle$ within a single self-assembled semiconductor QD (Fig. 1(a)). Two qubits are represented by the single exciton states $|10\rangle$ and $|01\rangle$ and the C-ROT operation is performed by implementing a π rotation on the first (target) qubit if and only if the second (control) qubit is in state 1. For the successful experimental implementation of optical control schemes employing pulse shaping techniques, it is essential that the quantum control system be well characterized using convenient, real-time pulse measurement tools.

Here, we report the experimental demonstration of the pulse shaping protocols found in Ref. 37 for C-ROT operations in quantum dots using a quantum control apparatus operating in the infrared spectral region (~1 eV, aimed at quantum dots with emission wavelengths in the 1.3 μm telecom band), in contrast to existing quantum control demonstrations in the visible and near infrared.[30–36] This apparatus is also used to assess the experimental limitations on gate fidelity due to inaccuracies in the pulse shaping system and other laser instabilities, indicating the feasibility of high fidelity (~0.99) quantum operations with a gate time (GT) below 1 ps with the implementation of pulse shaping. These findings thereby provide a useful benchmark in assessing noise limitations in more general quantum control applications using shaped optical pulses. In this work, the theoretical simulations in Ref. 37 are also extended to the application of shaping protocols to C-ROT operations on quantum dots of cylindrical symmetry, for which the exciton states are spin polarized, illustrating the universality of our approach. The pulse shapes were characterized using interferometric and noncollinear (zero-background) autocorrelation techniques as well as multiphoton intrapulse interference phase scan (MIIPS).[43,44] We find that the MIIPS trace exhibits unique visual signatures that would greatly aid in the implementation of real-time quantum control experiments. Our results lay the foundation required for the experimental implementation of general phase and amplitude pulse shaping protocols for application to a variety of quantum

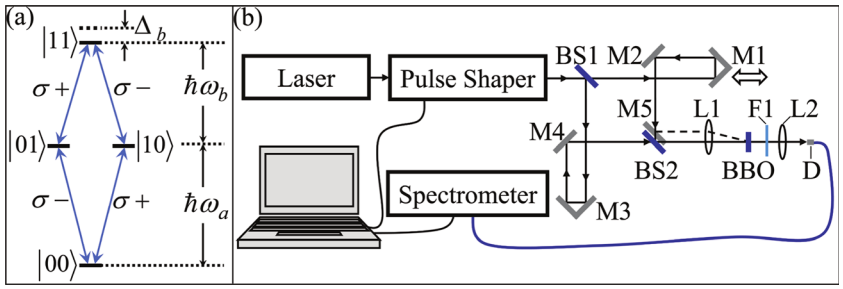

FIG. 1. (a) Energy level diagram showing excitonic transitions in semiconductor quantum dots with cylindrical symmetry. The system ground state (no excitons) is $|00\rangle$. Opposite circularly polarized light (represented by σ_+ and σ_-) leads to the generation of excitons with opposite spin ($|01\rangle$ and $|10\rangle$)). The biexciton state $|11\rangle$ consists of two excitons of opposite spin, with biexciton binding energy Δ_b. (b) Schematic diagram of the portion of the quantum control apparatus used to generate and characterize the pulse shaping protocols. Femtosecond pulses from the laser enter the pulse shaper where amplitude or phase masks are implemented on TL pulses. The shaped pulses enter the interferometric/non-collinear autocorrelator. Mirror M1 is mounted on a speaker driven by a function generator, proving a rapid scan delay line. The retroreflected beam is focused using lens L1 into a BBO crystal for second harmonic generation. Mirror M5 (beamsplitter BS2) is used for noncollinear (interferometric) autocorrelation measurements. Filter F1 removes any remaining IR components. Detector D is a photomultiplier tube used to collect autocorrelation traces or an optical fiber input connected to a spectrometer, providing feedback to the pulse shaper.

processes in semiconductor quantum dots, including Rabi rotations,[38] adiabatic passage,[26,27,39] and schemes for dynamical decoupling.[40–42]

II. NUMERICAL PULSE SHAPE OPTIMIZATION FOR CONTROLLED ROTATIONS

The interaction between the four-level system in Fig. 1(a) and the applied laser field is described by the Hamiltonian $H_{\text{int}} = -\vec{\mu}\cdot\vec{E}(t)$, where $\vec{E}(t) = \frac{1}{2}\hat{\epsilon}E_0(t)[\exp(-i\omega t - i\varphi(t)) + \exp(i\omega t + i\varphi(t))]$ is the electric field of the pulse and $\vec{\mu}$ is the electric dipole moment operator. Femtosecond pulse shaping systems, which are readily available from a variety of commercial sources,[45] provide independent control over the temporal (or equivalently spectral) characteristics of the amplitude $E_0(t)$ and phase $\varphi(t)$ of the laser pulse. This ability to finely tune the optical field provides a flexible tool for manipulating the quantum control Hamiltonian H_{int}. In this work, we focus on a typical 4-f pulse shaper configuration,[29] in which the pulse characteristics are manipulated in the spectral domain using a mask $M(\omega)$ placed in the Fourier plane. The Fourier transform of an ultrafast pulse exiting the pulse shaping system is given by

$$\tilde{E}_{\text{out}}(\omega) = \tilde{E}_{\text{in}}(\omega)M(\omega), \tag{1}$$

where $\tilde{E}_{\text{in}}(\omega)$ is the Fourier transform of the transform-limited (TL) input pulse, for which $\varphi = 0$ and $E_0(t) = |E_0|\text{sech}(1.76t/\tau)$, with $\tau = 130\,\text{fs}$. The mask function $M(\omega)$ is imposed using a spatial light modulator (SLM) and has the general form

$$M(\omega) = A_M(\omega)\exp[i\Phi_M(\omega)]. \tag{2}$$

Dual mask SLMs provide independent control of $A_M(\omega)$ and $\Phi_M(\omega)$. In this work, we apply the phase-only and amplitude-only shaping protocols developed in Ref. 37 to the C-ROT operation on spin-polarized exciton qubits, as depicted in Fig. 1(a). Circularly polarized selection rules (and degenerate $|01\rangle$ and $|10\rangle$ single exciton states) occur in cylindrically symmetric quantum dots. The corresponding level scheme for excitons and biexcitons in elongated quantum dots exhibiting linearly polarized optical selection rules and a nonzero exchange splitting between the single exciton states (typically $\sim 100\,\mu\text{eV}$) was considered in Ref. 37. The exciton dipole moment, the ground state exciton energy, and the biexciton binding energy were chosen to reflect typical values measured in experiments.[46,47] The amplitude-only shaping mask is given by

$$A_M(\omega) = \left|\exp\left[-\left(\frac{\omega-\omega_b}{\Delta\omega_1/(2\ln 2)^{1/2}}\right)^2\right] - A_0\exp\left[-\left(\frac{\omega-\omega_a}{\Delta\omega_2/(2\ln 2)^{1/2}}\right)^2\right]\right|, \tag{3}$$

where $E_a = \hbar\omega_a$ and $E_b = \hbar\omega_b$ are the transition energies from $|00\rangle$ to $|10\rangle$ and from $|01\rangle$ to $|11\rangle$, $\Delta\omega_1$ and $\Delta\omega_2$ are the Gaussian function bandwidths and A_0 is an amplitude factor. In this case, $\Phi_M(\omega)$ from Eq. (2) is set to zero for simplicity. The phase-only shaping mask is given by

$$\Phi_M(\omega) = \alpha\cos[\gamma(\omega-\omega_b) - \varphi]. \tag{4}$$

The fidelity of the C-ROT operation was maximized by varying $\Delta\omega_1$, $\Delta\omega_2$, A_0 (amplitude shaping scheme) or α, γ, and φ (phase shaping scheme) as well as the pulse area $\Theta = (\mu\cdot\hat{\epsilon}/\hbar)\int_{-\infty}^{+\infty}E_0(t)dt$. The constraints on the free parameters are the same as in Ref. 37 except that the initial TL pulse duration is taken to be 130 fs (corresponding to the full-width-at-half-maximum (FWHM) of the experimental pulses) and Θ was allowed to vary up to 8π radians, reflecting experimentally accessible values.[48] The chosen constraints ensure that $A_M(\omega)$ and $\Phi_M(\omega)$ are sufficiently slowly varying to be implemented with high accuracy on a standard 128 pixel SLM. Only the fidelity associated with the C-ROT gate is considered here: a fidelity of unity tied to quantum state initialization is assumed. The quantum state dynamics are calculated using the rotating-wave approximation. Details of the numerical optimization routine are provided in Ref. 37.

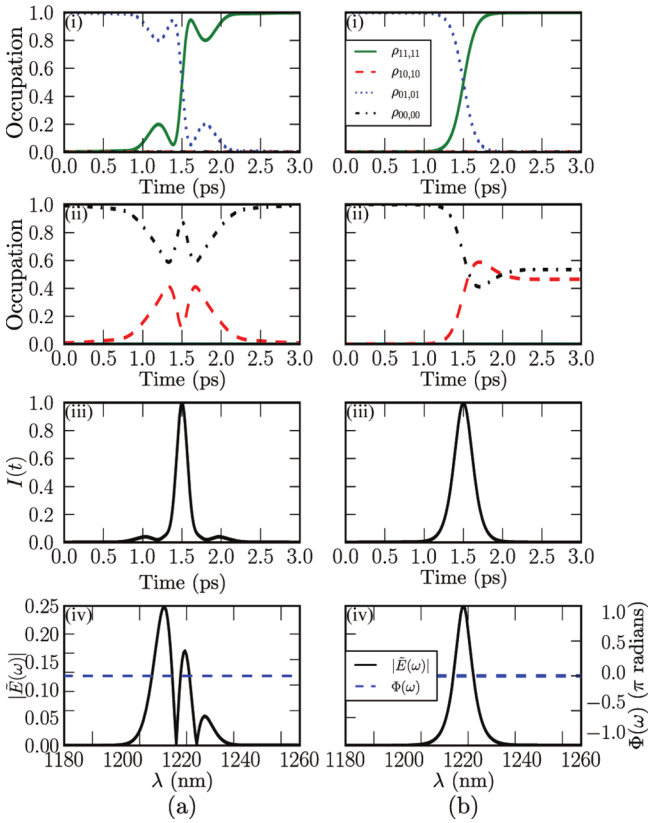

FIG. 2. Occupation dynamics and pulse characteristics for: (a) the optimum amplitude-shaped control pulse and (b) the TL pulse with equivalent gate time ($\Delta_b = 2.5$ meV). Panels (i) and (ii) indicate the state dynamics for initial occupation in $|01\rangle$ and $|00\rangle$, respectively. Only transitions coupled to the laser field are shown. Panels (iii) and (iv) show the temporal and spectral characteristics of the optical pulses.

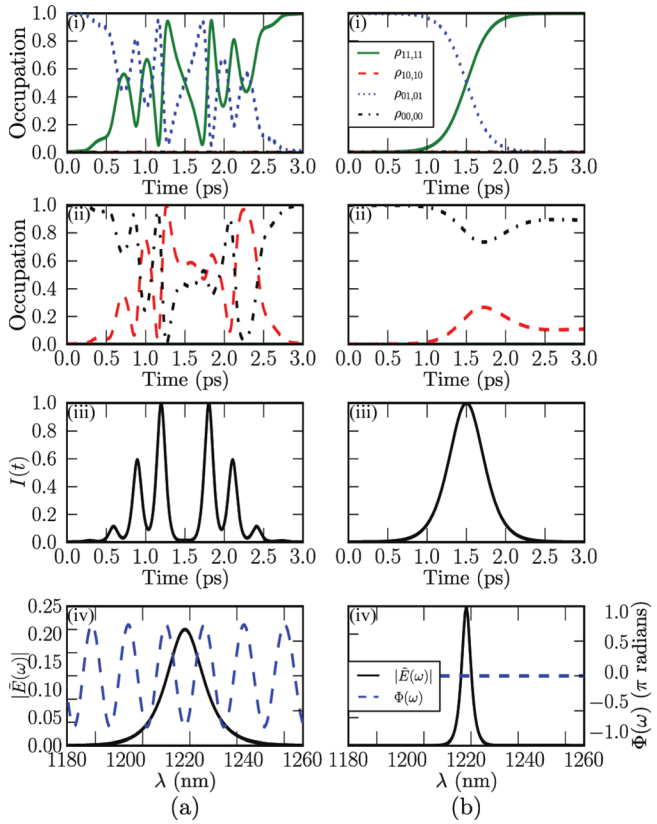

FIG. 3. Occupation dynamics and pulse characteristics for: (a) the optimum phase-shaped control pulse and (b) the TL pulse with equivalent gate time ($\Delta_b = 2.5$ meV). Panels (i) and (ii) indicate the state dynamics for initial occupation in $|01\rangle$ and $|00\rangle$, respectively. Only transitions coupled to the laser field are shown. Panels (iii) and (iv) show the temporal and spectral characteristics of the optical pulses.

The results of simulations of the C-ROT gate are shown in Figs. 2(a) and 3(a) for the optimum amplitude-shaped and phase-shaped pulses, respectively. In each case, the gate performance is compared to that for an unshaped (TL) pulse with an equivalent gate time.[49] The shaped pulses substantially outperform the unshaped pulses for both phase and amplitude shaping protocols, leading to the intended final system state for initial conditions corresponding to unity occupation of each of the four basis states. In contrast, for the TL pulses, there is an undesired change in the system state at the end of the pulse when the system is initially in $|00\rangle$ or $|10\rangle$. The shaped pulses therefore provide a much higher gate fidelity, corresponding to 0.999995 (amplitude-shaped pulse) and 0.999998 (phase-shaped pulse). The fidelities for the unshaped pulses are much lower (0.767445 and 0.944764 for the results in Figs. 2(b) and 3(b), respectively). The inclusion of relaxation using measured recombination and dephasing times in similar quantum dots[50] reduces our calculated fidelities by ≤ 0.004, reflecting a key advantage of the subpicosecond gate times considered here. The poor performance of the TL pulses is due to the lack of spectral selectivity between the $|00\rangle$ to $|10\rangle$ and $|01\rangle$ to $|11\rangle$ optical transitions, which are both strongly driven (in phase) by separate spectral components within the bandwidth of the optical pulse. In contrast, engineering the control Hamiltonian using pulse shaping allows one to tailor the evolution of the quantum state of the system. In this case, transient dynamics can occur during the laser pulse, but the desired system state is attained at the end of the quantum operation.

Figure 4(a) shows the variation of gate fidelity with biexciton binding energy (Δ_b). The fidelity increases with Δ_b in all cases, reflecting the relaxed constraints on the C-ROT performance due to the increasing energy difference between the $|00\rangle$ to $|10\rangle$ and $|01\rangle$ to $|11\rangle$ optical transitions. The fidelities saturate close to unity for both shaping schemes for $\Delta_b > 2.5$ meV, although the amplitude-shaped pulses provide higher fidelities for Δ_b between 1.0 meV and 2.0 meV. The gate times for the optimized pulses are shown in Fig. 4(b).

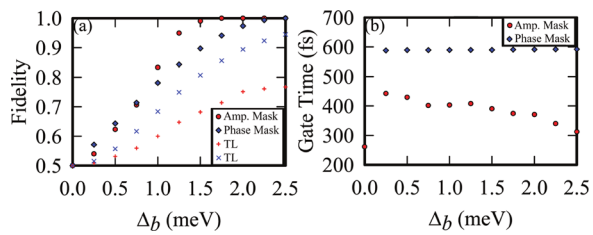

FIG. 4. (a) Gate fidelity of optimal phase-shaped (diamond), amplitude-shaped (circle), and TL pulses with equivalent gate times for both phase ($\times$) and amplitude ($+$) cases as a function of biexciton binding energy. (b) Gate time of optimized phase-shaped (diamond) and amplitude-shaped (circle) pulses as a function of biexciton binding energy.

The operation times for the phase shaping protocol are up to 50% longer than the gate times for the amplitude-shaped pulses, reflecting the complex shape of the temporal envelope associated with the simple phase-shaping mask function used here. Summaries of the optimized amplitude and phase mask parameters are given in Tables I and II, respectively.

III. EXPERIMENTAL IMPLEMENTATION OF OPTIMIZED PULSE SHAPES

A. Quantum control apparatus

Previous work in quantum control has involved optical sources and experiments in the visible or near-infrared spectral region.[30–36] As a result, the majority of development efforts for pulse shaping systems and pulse characterization equipment have been focused on this wavelength range. Self-assembled In(Ga)As quantum dots offer considerable flexibility for quantum computing applications due to the ability to fabricate ordered quantum dot arrays and composite microstructures.[51,52] The ground state optical transition in these quantum dots typically occurs in the range 0.8–1.1 eV.[46,47,53,54] The implementation of optically controlled quantum gates on exciton or spin states in these quantum dots therefore necessitates the development of a quantum control apparatus and suitable characterization tools operating in the infrared. A schematic diagram of the portion of the quantum control apparatus used for implementing the amplitude and phase shaping protocols and characterizing the resulting pulse shapes is shown in Fig. 1(b). The optical source is an optical parametric oscillator (OPO) that is synchronously pumped by a mode-locked Ti:sapphire oscillator. The center wavelength of the OPO pulses was tuned to the $|01\rangle$ to $|11\rangle$ transition. The ground state optical transition ($|00\rangle$ to $|10\rangle$) occurs at 1215 nm.[46] The biexciton binding energy was allowed to vary, as in the theoretical calculations. The programmable pulse shaping system utilizes a 128 pixel dual-mask SLM in the Fourier plane to apply amplitude or phase masks to the incident pulses. The shaped pulses were characterized using both interferometric and noncollinear autocorrelation measurements using the same apparatus, as shown in Fig. 1(b). The second harmonic (SH) signals were generated in a β-barium borate (BBO) crystal and detected by a photomultiplier tube. In order to implement MIIPS, the photomultiplier was replaced by an optical fiber input and fed into a spectrometer. The second harmonic spectrum simultaneously provides feedback to the pulse shaper and measurement of the real-time MIIPS trace.

TABLE I. Optimum pulse parameters, including operation GT, obtained for the amplitude shaping protocol for a range of biexciton binding energies.

Δ_b (meV)	F	$\hbar\Delta\omega_1$(meV)	$\hbar\Delta\omega_2$(meV)	A_0	Θ (π rad)	GT (fs)
0.00	0.500	9.921	12.463	0.387	1.531	261.7
0.25	0.539	6.188	6.426	0.902	7.930	442.6
0.50	0.623	6.083	6.877	0.915	8.000	429.5
0.75	0.706	6.083	7.158	0.921	8.000	401.8
1.00	0.833	6.083	7.550	0.947	8.000	403.2
1.25	0.949	6.083	7.928	0.937	8.000	407.9
1.50	0.990	6.083	8.118	0.941	8.000	390.5
1.75	0.999	6.408	8.830	0.939	7.995	374.6
2.00	1.000	6.086	9.209	0.908	6.231	370.9
2.25	1.000	6.741	10.555	0.904	6.185	340.0
2.50	1.000	7.475	12.068	0.903	6.410	312.3

TABLE II. Optimum pulse parameters, including operation GT, obtained for the phase shaping protocol for a range of biexciton binding energies.

Δ_b (meV)	F	α (π rad)	γ (fs)	φ (π rad)	Θ (π rad)	GT (fs)
0.00	0.500	1.000	303.8	1.000	3.471	773.5
0.25	0.571	0.737	304.3	−0.109	4.227	588.1
0.50	0.643	0.737	304.3	−0.100	4.233	589.1
0.75	0.714	0.736	304.3	−0.087	4.241	589.2
1.00	0.781	0.736	304.3	−0.075	4.242	589.4
1.25	0.843	0.735	304.3	−0.062	4.228	589.6
1.50	0.897	0.734	304.3	−0.050	4.223	589.6
1.75	0.941	0.734	304.3	0.962	4.219	590.7
2.00	0.974	0.734	304.3	−0.025	4.209	591.2
2.25	0.994	0.734	304.3	0.987	4.198	591.8
2.50	1.000	0.734	303.3	−1.000	4.185	592.0

B. Dispersion compensation

The output of a typical ultrafast laser system is not an ideal transform-limited pulse, even for a standard mode-locked femtosecond oscillator. When laser accessories such as optical parametric oscillators and regenerative amplifiers are used, the phase distortions become even larger. In addition, as a laser pulse travels through an experimental setup, dispersive optics further distort the pulse phase. The ability to apply the desired pulse shape precisely at the QD sample position, accounting for phase distortions accumulated from transit through the apparatus, is imperative. This requires an accurate measurement of the pulse phase so that appropriate dispersion compensation may be introduced. We employ a pulse shaping system equipped with MIIPS.[43,44] As MIIPS is a single beam technique, and is insensitive to the optical mode, it is readily implemented at the QD sample position after all dispersive optics in the apparatus, representing a significant advantage over other pulse characterization techniques for this type of application.[55,56] In order to implement MIIPS, the QD sample at the laser focus is replaced by a nonlinear crystal and the SH spectrum is measured using an optical fiber connected to a spectrometer (Fig. 1(b)). As described in Ref. 43, a sinusoidal reference phase function is imposed on the input pulses using the SLM and the SH spectrum is measured as a function of the phase argument (δ). Maxima in the resulting two-dimension plot of SH wavelength versus δ provide a measure of the second derivative of the pulse phase $\varphi''(\omega)$. Integration then provides $\varphi(\omega)$, which can be compensated using the SLM to obtain TL pulses. For completeness, the pulses in this work were also characterized using interferometric and zero-background autocorrelation techniques.

The results of pulse characterization before and after dispersion compensation are shown in Fig. 5. The FWHM of the zero-background autocorrelation trace before compensation is 398 fs, corresponding to a pulse duration, assuming a

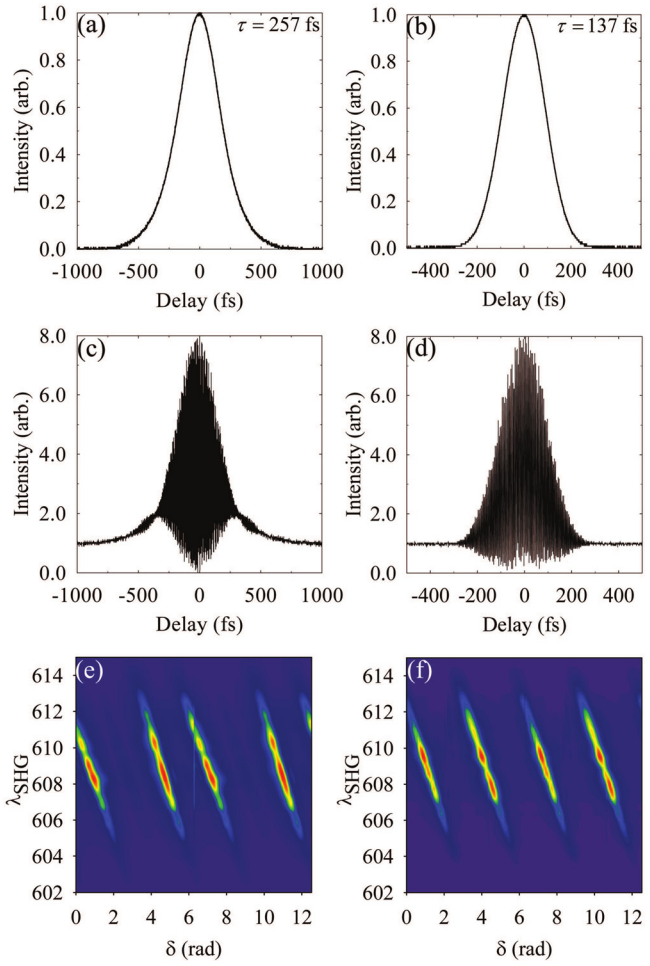

FIG. 5. Results of pulse characterization before ((a), (c), and (e)) and after ((b), (d), and (f)) the introduction of dispersion compensation using MIIPS. (a) and (b) show the results of noncollinear autocorrelation measurements; (c) and (d) show results of interferometric autocorrelation measurements; and (e) and (f) show the measured MIIPS traces.

hyperbolic secant shape, of 257 fs. After dispersion compensation, the pulse duration is reduced to 137 fs, indicating the removal of a substantial amount of phase distortion. (Note the difference in the range of the time delay axes on the left and right sides of Fig. 5.) The raised wings in the lower envelope of the interferometric autocorrelation in Fig. 5(c) is a characteristic signature of linear chirp (second-order phase distortion), indicating that this type of phase distortion dominates in the pulses prior to compensation. The observation of a clean TL interferometric autocorrelation in Fig. 5(d) indicates that these second-order phase distortions have been removed. The superior sensitivity to pulse chirp of the interferometric autocorrelation over the noncollinear autocorrelation comes at the expense of an increased complexity of optical alignment. The associated MIIPS traces are shown in Fig. 5(e) (before compensation) and Fig. 5(f) (after compensation). The results in Fig. 5(f) indicate evenly spaced (by π) parallel diagonal lines, as expected for a TL pulse.[43] The second-order phase distortion in the pulses prior to compensation is indicated in Fig. 5(e) by the appearance of unequal spacing between the lines. A small difference in the relative angle of the lines is also apparent in Fig. 5(e), reflecting a small amount of third-order phase distortion. In contrast, no residual phase distortion is apparent in the MIIPS trace for the compensated pulses (Fig. 5(f)). The dramatic difference between the pulse characterization results shown on the left and right sides of Fig. 5 emphasizes the essential role played by dispersion compensation in the implementation of optimized pulse shapes for quantum control experiments.

C. Shaped pulse characterization

The spectral and temporal characteristics of the shaped pulses are shown in Fig. 6 for the optimum pulse parameters corresponding to a biexciton binding energy of 2.5 meV (see Tables I and II). It is evident from Fig. 6(a) that the amplitude mask leads to a large overall reduction in the total pulse

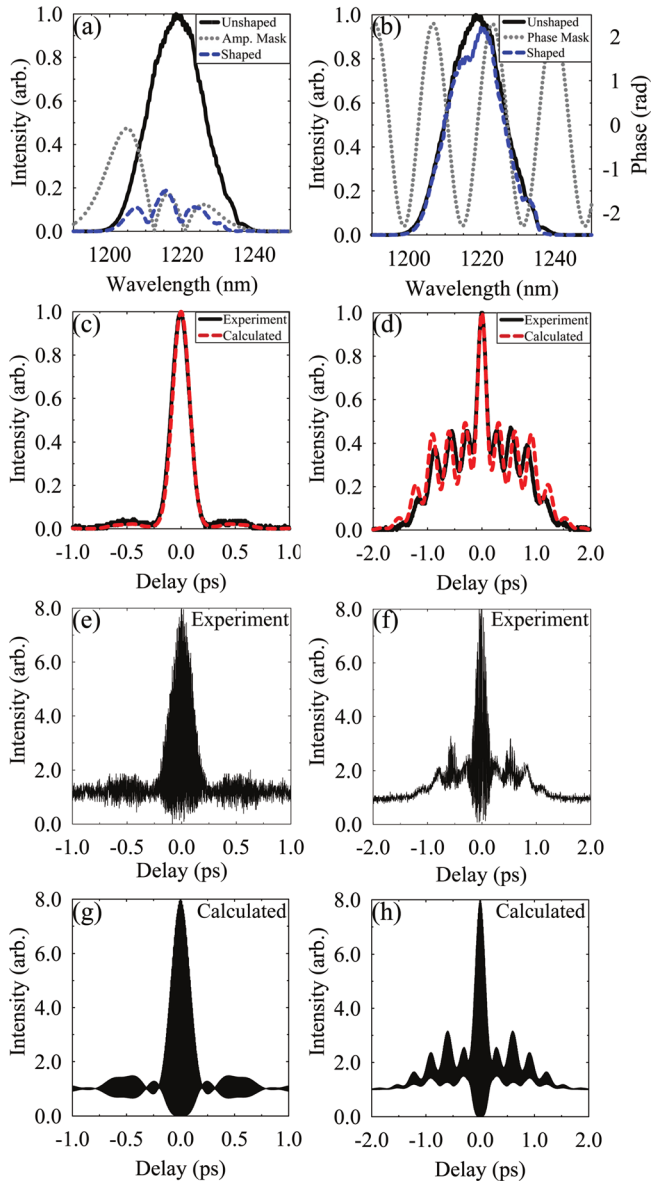

FIG. 6. Shaped pulse characteristics for the optimized control pulses ($\Delta_b = 2.5$ meV). Results for the amplitude-shaped pulses are shown on the left ((a), (c), (e), and (g)) and the phase-shaped pulses are shown on the right ((b), (d), (f), and (h)). (a), (b) Measured laser spectrum before and after application of the shaping mask; (c), (d) measured and calculated zero-background autocorrelations of shaped pulses; (e), (f) measured interferometric autocorrelations of the shaped pulses; (g), (h) calculated interferometric autocorrelations of the shaped pulses.

area, representing an inefficient use of laser resources in the application of quantum control. In contrast, for the phase-shaping protocol, no loss of pulse area occurs in the ideal case. The characteristics of the shaped pulses in the temporal domain are presented in Figs. 6(c)–6(h). For each shaping protocol, the measured noncollinear and interferometric autocorrelations are shown together with corresponding calculated autocorrelation traces. These calculations were obtained by numerically imposing the shaping masks onto the experimental laser spectrum assuming the input pulses have zero initial phase at all wavelengths.[57] The application of the amplitude mask introduces temporal structure on the pulse that is manifested in the autocorrelation traces through the appearance of weak shoulders. The phase-shaped pulse exhibits a complex temporal profile, leading to an autocorrelation trace with an oscillatory structure, as seen in Figs. 6(d) and 6(f).

Measurements of the pulse autocorrelation and spectrum provide an accurate real-time characterization tool for verifying the proper application of the shaping protocols during quantum control experiments. The need for stable spatial and temporal overlap of the two beams in the autocorrelator at the BBO crystal nevertheless makes this approach highly sensitive to drifts in the optical system. In addition, duplication of much of the optical setup is required in order to create an equivalent focus to the sample position at the location in the setup where the autocorrelator is placed. This equivalent focus is needed to accurately reproduce the dispersion effects of all optical elements in the setup. Measurements of the shaped pulse characteristics using MIIPS were also performed to gauge the sensitivity of this technique to the mask parameters. The MIIPS traces corresponding to the shaped pulses in Fig. 6 are shown in Fig. 7. Calculated MIIPS traces are also shown, for comparison. The observation of equally spaced parallel lines in the MIIPS trace for the amplitude-shaped pulse in Fig. 7(a) verifies that the spectral phase profile is constant. This information is apparent from the MIIPS trace without the need for additional analysis, unlike the autocorrelation traces in Figs. 6(c) and 6(e). The severe restriction in the transmitted optical power through the shaper as a result of the imposed amplitude mask limits the signal-to-noise ratio. It is clear from the measured results in Fig. 7(b) that the phase mask leads to a dramatic change in the measured MIIPS trace when compared to the corresponding TL result in Fig. 5(f). The appearance of a cross hatch pattern is reflective of the nonlinearity of the sinusoidal phase mask utilized for the phase shaping protocol. The calculated MIIPS traces in Figs. 7(c) and 7(d) provide good agreement with the measured MIIPS data.

The sensitivity of the MIIPS trace to the mask parameters for the phase-shaping protocol is illustrated in Fig. 8, where the measured MIIPS results are shown as a function of Δ_b. These traces all show a cross hatch pattern, however, the locations on the trace where the intensity is a maximum varies for different values of Δ_b. It is clear from the pulse parameters in Table II that the optimum values of α and γ are approximately constant for all Δ_b. The variations in the visual features in the MIIPS traces in Fig. 8 are therefore

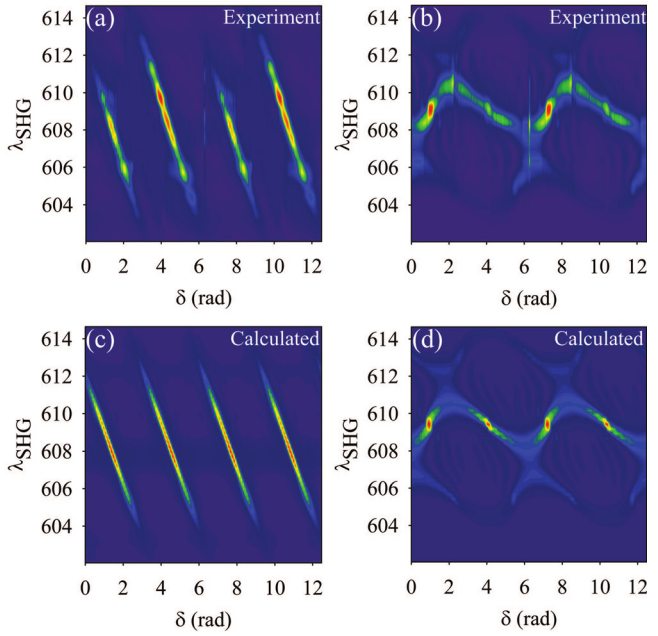

FIG. 7. Measured MIIPS traces of (a) amplitude-shaped and (b) phase-shaped control pulses. Calculated MIIPS trace of (c) amplitude-shaped and (d) phase-shaped control pulses ($\Delta_b = 2.5$ meV).

tied to variations in φ. In order to gain more insight into the dependence of the features in the MIIPS trace on the mask parameters, we performed numerical simulations for a wide range of values of α, γ, and φ. These simulations show that α and γ have similar effect on the trace. As the magnitude of either α or γ is increased from zero, the trace evolves from parallel lines (TL case) to a cross hatch pattern. Further increasing the magnitude then leads to dissociation into modulated horizontal lines. This dependence may be seen by comparing the MIIPS traces in Figs. 8(a) and 8(e), which have different values of α. As φ is varied from $-\pi$ to π, the cross hatch pattern shifts diagonally to the lower right in the MIIPS trace, and the relative intensity of alternating cross points reverses twice. Variations in φ also lead to changes in the asymmetry of the bright regions, as evident in the MIIPS results in Fig. 8. The high sensitivity of the MIIPS trace to the mask parameters for the phase-shaping protocol makes it an excellent real-time diagnostic tool in quantum control experiments on semiconductor quantum dots.

IV. EXPERIMENTAL LIMITS ON QUANTUM GATE PERFORMANCE

The pulse characterization results in Secs. III B and III C have allowed the authors to quantify the experimental limits on the fidelity of the C-ROT gate considered here. As other quantum processes (such as adiabatic rapid passage) are likely to be less sensitive than the C-ROT to sources of noise, the calculated gate errors obtained from our detected uncertainties represent a worst-case scenario for quantum control. There are three dominant sources of error: (i) an uncertainty in the implementation of the desired pulse shape; (ii) pulse to pulse intensity fluctuations; and (iii) fluctuations

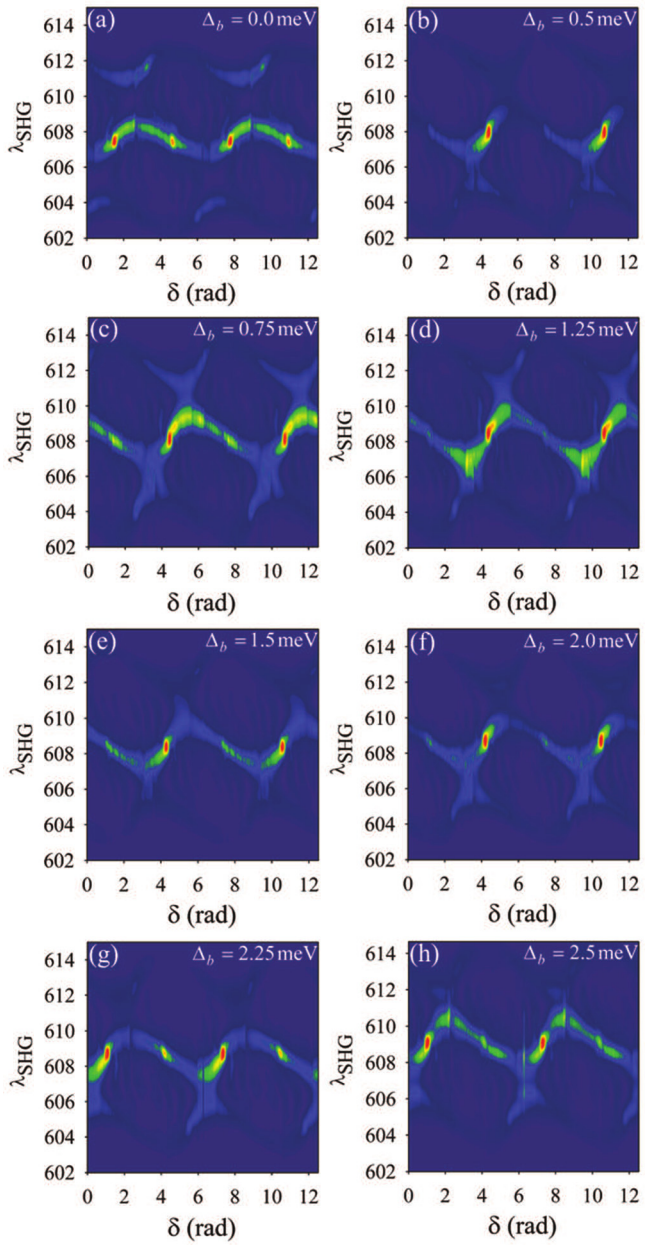

FIG. 8. Measured MIIPS traces of phase-shaped control pulses for various values of Δ_b. The mask parameters at each Δ_b are listed in Table II.

in the center wavelength. (We note that some degree of spatial chirp is occasionally detected in the experimental MIIPS traces (e.g., Fig. 7), however, this does not represent a fundamental limitation unlike the other effects listed above.[58]) Numerical simulations of the C-ROT gate were performed to determine the gate error associated with each of the above effects. The resulting changes in the gate fidelity are shown in Table III. For these simulations, the error associated with (i) was estimated from the measured accuracy of dispersion compensation, as this takes into account both the uncertainty in the calibration of the SLM and the measurement of the pulse phase prior to compensation. Using the MIIPS compensation approach (with a total of six iterations), a typical value for the ratio between the measured pulse duration τ (after compensation but before shaping) and the theoretical pulse duration τ_{TL} (based on the measured pulse bandwidth) is 1.002 indicating a small deviation from the transform-limit. The uncertainty in the imposed phase and amplitude mask was then modeled by including an unintended residual chirp in the phase profile[59] and an associated percentage change in the amplitude mask. Fluctuations in the pulse to pulse intensity reflect the stability of the OPO laser source used in this work, and are $<0.5\%$. Due to the active feedback of the cavity length, the center wavelength typically fluctuates over the range ± 0.2 nm.

TABLE III. Calculated change in fidelity for the C-ROT gate associated with different sources of error determined from the measured pulse characteristics. The deviation from the ideal pulse shape is estimated using the ratio $\tau/\tau_{TL} = 1.002$, which describes the accuracy of the applied dispersion compensation. Peak to peak pulse fluctuations (0.5%) and wavelength instabilities (± 0.2 nm) reflect the characteristics of the OPO used in our experiments and may not represent fundamental limits.

Source of error	Amplitude mask	Phase mask
Pulse shape inaccuracy	0.0034	0.0096
Peak to peak intensity fluctuations	0.00002	0.0002
Wavelength instability	0.0008	0.011

It should be noted that the implementation of dispersion compensation (using MIIPS or other approaches) requires an accurate measurement of the pulse characteristics at the sample position, or at an equivalent focus. In this work, we envision quantum hardware incorporating one or more quantum dots in a lateral microcavity,[7,11] possibly extendable to an array of such cavities coupled by optical waveguides.[13] Our estimated uncertainties in the pulse shape implementation are appropriate for optical excitation parallel to the growth direction in such a configuration provided that an anti-reflection coated wafer is employed. The use of a structure incorporating a vertical microcavity would require a separate analysis of the sources of error taking into account pulse propagation effects. We note that the quantum dot selection rules do not represent a significant source of error as we have shown that the shaping protocols are effective in both cases of cylindrically symmetric and elongated quantum dots.

The results in Table III indicate that the C-ROT fidelity is more sensitive to sources of error for the phase mask than for the amplitude mask. This is likely due to the fact that the total pulse area is an adjustable parameter in the optimization routine, and for the optimum phase mask, the pulse area induces multiple Rabi rotations. It may be possible to reduce these sensitivities through use of a different mask function for the phase profile, however, our analysis was limited in this work to the mask function in Eq. (4). The influences of experimental error are in all cases $\sim 1\%$ or less, comparable to the effects of decoherence, as discussed in Sec. II and in Ref. 37. These results reinforce the feasibility of high-fidelity quantum operations in semiconductor quantum dots.

V. CONCLUSIONS

The application of pulse shaping protocols in infrared quantum control experiments on semiconductor quantum dots is investigated. Numerically optimized pulse shapes for C-ROT operations on exciton qubits are implemented in a

4-f pulse shaper geometry using an apparatus operating at ~1 eV, matching the optical transitions of In(Ga)As self-assembled quantum dots. Our pulse characterization results show that accurate dispersion compensation is essential to achieve the desired pulse shapes at the quantum dot sample, and that MIIPS provides a sensitive real-time diagnostic tool in these experiments. Our findings are used to evaluate reductions in fidelity associated with imperfections in the pulse shaping system and other noise sources, indicating that these effects lead to only ~1% change, comparable to the effects of decoherence. These results indicate that high fidelity operations in semiconductor quantum dots are readily achievable with a gate time below 1 ps with the implementation of pulse shaping techniques, laying the foundation for the application of these techniques to a variety of other quantum processes.

ACKNOWLEDGMENTS

This research is supported by the Canadian Foundation for Innovation, the Natural Sciences and Engineering Research Council of Canada, the Canada Research Chairs Program, Rockwell Collins, and Lockheed Martin Corporation.

[1]D. Loss and D. P. DiVincenzo, Phys. Rev. A **57**, 120 (1998).
[2]E. Biolatti, R. C. Iotti, P. Zanardi, and F. Rossi, Phys. Rev. Lett. **85**, 5647 (2000).
[3]F. Troiani, U. Hohenester, and E. Molinari, Phys. Rev. B **62**, R2263 (2000).
[4]P. Chen, C. Piermarocchi, and L. J. Sham, Phys. Rev. Lett. **87**, 067401 (2001).
[5]J. H. Reina, L. Quiroga, and N. F. Johnson, Phys. Rev. A **62**, 012305 (2000).
[6]C. Piermarocchi, P. Chen, Y. S. Dale, and L. J. Sham, Phys. Rev. B **65**, 075307 (2002).
[7]A. Imamoğlu, D. D. Awschalom, G. Burkard, D. P. DiVincenzo, D. Loss, M. Sherwin, and A. Small, Phys. Rev. Lett. **83**, 4204 (1999).
[8]C. Piermarocchi, P. Chen, L. J. Sham, and D. G. Steel, Phys. Rev. Lett. **89**, 167402 (2002).
[9]F. Troiani, E. Molinari, and U. Hohenester, Phys. Rev. Lett. **90**, 206802 (2003).
[10]S. E. Economou, L. J. Sham, Y. Wu, and D. G. Steel, Phys. Rev. B **74**, 205415 (2006).
[11]T. A. Brun and H. Wang, Phys. Rev. A **61**, 032307 (2000).
[12]L. Quiroga and N. F. Johnson, Phys. Rev. Lett. **83**, 2270 (1999).
[13]S. M. Clark, K.-M. C. Fu, T. D. Ladd, and Y. Yamamoto, Phys. Rev. Lett. **99**, 040501 (2007).
[14]T. H. Stievater, X. Li, D. G. Steel, D. Gammon, D. S. Katzer, D. Park, C. Piermarocchi, and L. J. Sham, Phys. Rev. Lett. **87**, 133603 (2001).
[15]A. Zrenner, E. Beham, S. Stufler, F. Findeis, M. Bichler, and G. Abstreiter, Nature **418**, 612 (2002).
[16]H. Kamada, H. Gotoh, J. Temmyo, T. Takagahara, and H. Ando, Phys. Rev. Lett. **87**, 246401 (2001).
[17]H. Htoon, T. Takagahara, D. Kulik, O. Baklenov, A. L. Holmes, and C. K. Shih, Phys. Rev. Lett. **88**, 087401 (2002).
[18]P. Borri, W. Langbein, S. Schneider, U. Woggon, R. L. Sellin, D. Ouyang, and D. Bimberg, Phys. Rev. B **66**, 081306 (2002).
[19]T. Flissikowski, A. Betke, I. A. Akimov, and F. Henneberger, Phys. Rev. Lett. **92**, 227401 (2004).
[20]S. Stufler, P. Machnikowski, P. Ester, M. Bichler, V. M. Axt, T. Kuhn, and A. Zrenner, Phys. Rev. B **73**, 125304 (2006).
[21]D. Press, T. D. Ladd, B. Zhang, and Y. Yamamoto, Nature **456**, 218 (2008).
[22]B. D. Gerardot, D. Brunner, P. A. Dalgarno, P. Ohberg, S. Seidl, M. Kroner, K. Karrai, N. G. Stoltz, P. M. Petroff, and R. J. Warburton, Nature **451**, 441 (2008).
[23]X. Li, Y. Wu, D. Steel, D. Gammon, T. H. Stievater, D. S. Katzer, D. Park, C. Piermarocchi, and L. J. Sham, Science **301**, 809 (2003).
[24]S. J. Boyle, A. J. Ramsay, F. Bello, H. Y. Liu, M. Hopkinson, A. M. Fox, and M. S. Skolnick, Phys. Rev. B **78**, 075301 (2008).
[25]G. Chen, N. H. Bonadeo, D. G. Steel, D. Gammon, D. S. Katzer, D. Park, and L. J. Sham, Science **289**, 1906 (2000).
[26]Y. Wu, I. M. Piper, M. Ediger, P. Brereton, E. R. Schmidgall, P. R. Eastham, M. Hugues, M. Hopkinson, and R. T. Phillips, Phys. Rev. Lett. **106**, 067401 (2011).
[27]C.-M. Simon, T. Belhadj, B. Chatel, T. Amand, P. Renucci, A. Lemaitre, O. Krebs, P. A. Dalgarno, R. J. Warburton, X. Marie, and B. Urbaszek, Phys. Rev. Lett. **106**, 166801 (2011).
[28]Y. Wu, X. Li, L. M. Duan, D. G. Steel, and D. Gammon, Phys. Rev. Lett. **96**, 087402 (2006).
[29]A. M. Weiner, Rev. Sci. Instrum. **71**, 1929 (2000).
[30]D. Meshulach and Y. Silberberg, Nature **396**, 239 (1998).
[31]S. Zhdanovich, E. A. Shapiro, M. Shapiro, J. W. Hepburn, and V. Milner, Phys. Rev. Lett. **100**, 103004 (2008).
[32]B. Broers, H. B. van Linden van den Heuvell, and L. D. Noordam, Phys. Rev. Lett. **69**, 2062 (1992).
[33]B. Chatel, J. Degert, S. Stock, and B. Girard, Phys. Rev. A **68**, 041402 (2003).
[34]J. S. Melinger, S. R. Gandhi, A. Hariharan, D. Goswami, and W. S. Warren, J. Chem. Phys. **101**, 6439 (1994).
[35]P. Brumer and M. Shapiro, Ann. Rev. Phys. Chem. **43**, 257 (1992).
[36]H. Rabitz, R. de Vivie-Riedle, M. Motzkus, and K. Kompa, Science **288**, 824 (2000).
[37]R. Mathew, C. E. Pryor, M. E. Flatté and K. C. Hall, Phys. Rev. B **84**, 205322 (2011).
[38]G. Chen, T. H. Stievater, E. T. Batteh, X. Li, D. G. Steel, D. Gammon, D. S. Katzer, D. Park, and L. J. Sham, Phys. Rev. Lett. **88**, 117901 (2002).
[39]H. Y. Hui and R. B. Liu, Phys. Rev. B **78**, 155315 (2008).
[40]P. Karbach, S. Pasini, and G. S. Uhrig, Phys. Rev. A **78**, 022315 (2008).
[41]T. E. Hodgson, L. Viola, and I. D'Amico, Phys. Rev. B **78**, 165311 (2008).
[42]V. M. Axt, P. Machnikowski, and T. Kuhn, Phys. Rev. B **71**, 155305 (2005).
[43]V. V. Lozovoy, I. Pastirk, and M. Dantus, Opt. Lett. **29**, 775 (2004).
[44]B. Xu, J. M. Gunn, J. M. D. Cruz, V. V. Lozovoy, and M. Dantus, J. Opt. Soc. Am. B **23**, 750 (2006).
[45]Commercial pulse shaper systems are available, for example, from Coherent Inc., Biophotonic Solutions Inc., and Fastlite. The system used in this work was custom designed and fabricated for the infrared spectral region by BioPhotonic Solutions Inc.
[46]K. L. Silverman, R. P. Mirin, S. T. Cundiff, and A. G. Norman, Appl. Phys. Lett. **82**, 4552 (2003).
[47]C. Dal Savio, K. Pierz, G. Ade, H. Danzebrink, E. Göbel, and A. Hangleiter, Appl. Phys. B: Lasers Opt. **84**, 317 (2006).
[48]A. J. Ramsay, T. M. Godden, S. J. Boyle, E. M. Gauger, A. Nazir, B. W. Lovett, A. M. Fox, and M. S. Skolnick, Phys. Rev. Lett. **105**, 177402 (2010).
[49]The gate time for a given excitation pulse was determined by normalizing the intensity profile and determining the width of a normalized square pulse with the same total area.
[50]P. Borri, W. Langbein, S. Schneider, U. Woggon, R. L. Sellin, D. Ouyang, and D. Bimberg, Phys. Rev. Lett. **87**, 157401 (2001).
[51]H. Heidemeyer, U. Denker, C. Müller, and O. G. Schmidt, Phys. Rev. Lett. **91**, 196103 (2003).
[52]E. Peter, P. Senellart, D. Martrou, A. Lemaître, J. Hours, J. M. Gérard, and J. Bloch, Phys. Rev. Lett. **95**, 067401 (2005).
[53]T. Yang, O. Shchekin, J. D. O'Brien, and D. G. Deppe, Electron. Lett. **39**, 1657 (2003).
[54]D. Dalacu, D. Poitras, J. Lefebvre, P. J. Poole, G. C. Aers, and R. L. Williams, Appl. Phys. Lett. **82**, 4803 (2003).
[55]R. Trebino, K. W. DeLong, D. N. Fittinghoff, J. N. Sweetser, M. A. Krumbügel, B. A. Richman, and D. J. Kane, Rev. Sci. Instrum. **68**, 3277 (1997).
[56]C. Iaconis and I. A. Walmsley, Opt. Lett. **23**, 792 (1998).
[57]Calculations of autocorrelation and MIIPS traces were done by importing the measured laser spectrum into a commercial pulse shaping program, femtoPulse Master, purchased from Biophotonic Solutions Inc.
[58]Spatial chirp may be manifested in MIIPS as a difference in the amplitude of the signal for $\delta = 0$ to π and $\delta = \pi$ to 2π, as seen for example in Fig. 7. These effects are likely tied to the sensitivity of the OPO mode profile to tuning, and were only observed occasionally.
[59]A. E. Siegman, *Lasers* (University Science Books, Sausalito, 1986).